Computer Vision and Image Understanding 146 (2016) 52–66

Contents lists available at ScienceDirect

Computer Vision and Image Understanding

journal homepage: www.elsevier.com/locate/cviu

Stereo fusion: Combining refractive and binocular disparity

Seung-Hwan Baek, Min H. Kim*

KAIST, 291 Daehak-ro, Yuseong-gu, Daejeon, South Korea

ARTICLE INFO

Article history:
Received 26 February 2015
Accepted 6 February 2016

Keywords:
Stereo fusion
Refractive stereo
Multi-view stereo

ABSTRACT

The performance of depth reconstruction in binocular stereo relies on how adequate the predefined baseline for a target scene is. Wide-baseline stereo is capable of discriminating depth better than the narrow-baseline stereo, but it often suffers from spatial artifacts. Narrow-baseline stereo can provide a more elaborate depth map with fewer artifacts, while its depth resolution tends to be biased or coarse due to the short disparity. In this paper, we propose a novel optical design of heterogeneous stereo fusion on a binocular imaging system with a refractive medium, where the binocular stereo part operates as wide-baseline stereo, and the refractive stereo module works as narrow-baseline stereo. We then introduce a stereo fusion workflow that combines the refractive and binocular stereo algorithms to estimate fine depth information through this fusion design. In addition, we propose an efficient calibration method for refractive stereo. The quantitative and qualitative results validate the performance of our stereo fusion system in measuring depth in comparison with homogeneous stereo approaches.

1. Introduction

There have been many approaches to acquiring depth information of real scenes such as passive stereo [1], active stereo [2], time-of-flight imaging [3], depth from defocus [4], etc. Among them, passive stereo imaging has been commonly used for distant measurements to understand scene shapes. Classical stereo algorithms employ a pair of binocular stereo images. Such stereo algorithms estimate depth by evaluating the distance of corresponding features, so-called disparity, via computing matching costs and aggregating the costs [1]. However, owing to the nature of triangulation in depth estimation, depth accuracy strongly depends on the baseline between a stereo pair. For instance, a wide baseline elongates the range of the correspondence search so that the matching problem cannot be solved with high precision in typical locally-optimizing approaches [5]. On the contrary, a narrow baseline shortens the resolution of disparity; therefore, the accuracy of estimated depth could be degraded [6,7].

Recently, Gao and Ahuja [8,9] introduced a single-depth camera based on refraction. Chen et al. [10] further extended this refractive mechanism. Such refractive stereo systems estimate depth from the change of light direction; therefore, the disparity in refractive stereo in general is smaller than that in binocular stereo, i.e., its performance is similar to that of binocular stereo with a narrow baseline.

We take inspiration from refractive stereo to combine these two heterogeneous stereo systems, where a stereo fusion system is designed with a refractive medium placed on one of the binocular stereo cameras. In this paper, we introduce a novel optical design that combines binocular and refractive stereo and its depth process workflow that allows us to fuse heterogeneous stereo inputs seamlessly to achieve fine depth estimates. Our system comprises a pair of stereo cameras, one of which is covered with a transparent medium, allowing for enhanced depth accuracy. The proposed approach offers benefits compared to the typical multiview stereo [7] in terms of building cost as our system employs just the same number of cameras as a binocular stereo does. It is also more advantageous than multiview stereo, which consists of two cameras on a linear slider [11], by providing physical stability, i.e., spinning the medium is less undemanding than moving a camera on the slider frequently at different distances.

The refractive calibration process that we propose in this paper is a natural evolution of our previously published research [12]. We increase the efficiency of the tedious refractive calibration process in the prior work [12]. In this paper, we propose a novel refractive calibration method that requires fewer angle samples (at least three angles), rather than the dense angle samples, from 0 to 360° at 10-degree intervals. As such, the novel calibration method can accelerate the cumbersome calibration process that hinders the usefulness of refractive stereo. We believe that this

* Corresponding author.
E-mail address: minhkim@kaist.ac.kr, minhkim@vclab.kaist.ac.kr (M.H. Kim).

http://dx.doi.org/10.1016/j.cviu.2016.02.006
1077-3142/

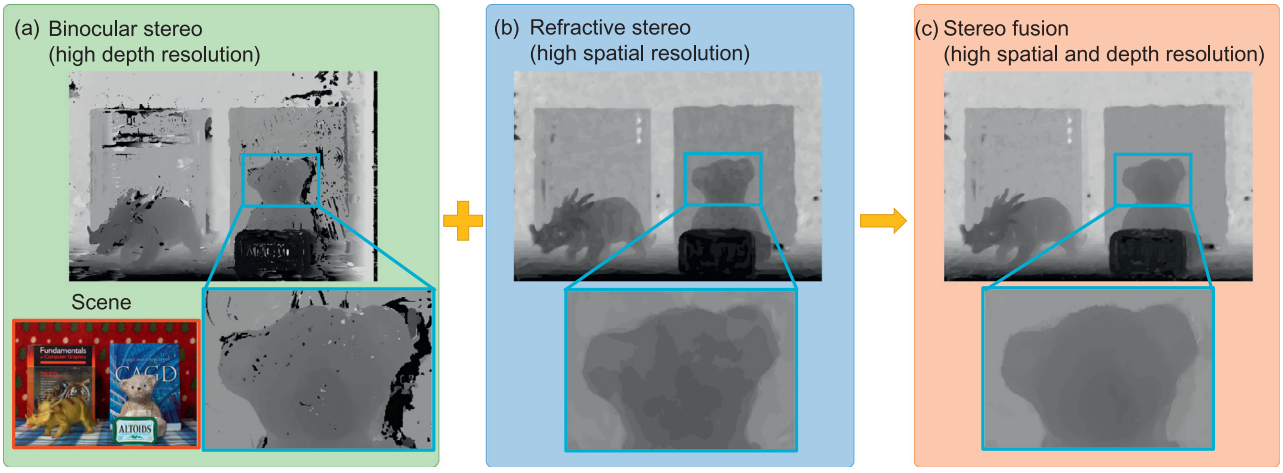

Fig. 1. (a) Binocular stereo detects depth accurately, whereas it suffers from spatial artifacts caused by occlusions and featureless regions. (b) Refractive stereo improves the spatial resolution with fewer artifacts, but its depth resolution is coarse with fewer steps. (c) Our stereo fusion significantly improves both spatial and depth resolution by combining these two heterogeneous stereo methods.

calibration method increases the usefulness of the proposed stereo fusion method.

Fig. 1 shows a brief overview of our method. The following contributions have been made:

- **A stereo fusion system that combines refractive and binocular stereo.** We propose a stereo fusion system that combines a refractive medium on a binocular base. The medium is placed in front of a camera in binocular stereo.
- **Calibration methods for stereo fusion.** We develop a workflow of calibration for this fusion system that includes radiometric, geometric and refractive calibration methods. In particular, we propose an efficient calibration method of refractive stereo based on xyz-Euler angles, which requires a smaller number of angle measurements (at least three angles), rather than dense measurements of complete angle variation. This calibration enables us to obtain the essential points of the entire angles from sub-sampled angle measurements.
- **Depth fusion workflow that combines two heterogeneous stereo images.** Our calibration methods allow us to estimate depth from two heterogeneous stereos. The resulting depth map achieves a higher depth resolution with fewer artifacts than that of traditional homogeneous stereo.

2. Binocular vs. refractive disparity

This section describes the foundational differences of binocular and refractive stereo, surveying state-of-the-art depth-from-stereo methods.

2.1. Multi-baseline stereo

Binocular disparity in stereo imaging describes pixel-wise displacement of parallax between corresponding points on a pair of stereo images taken from different positions. Searching correspondence on an epipolar line is necessary prior to computing disparity. As disparity d depends on its depth, we can recover the depth z using simple trigonometry as follows:

$$z = fb/d, \tag{1}$$

where f is the focal length of the camera lens, and b is the distance between the center of projections for the two cameras, the so-called baseline. In particular, the baseline b determines the depth resolution of the stereo system, and b is also related with occlusion error. Therefore, baseline must be adapted to the scene configuration for optimal performance. There is no universal configuration of baseline for real-world conditions.

Wide-baseline stereo reserves more pixels for disparity than narrow-baseline stereo does. Therefore, wide-baseline systems can discriminate depth with a higher resolution. On the other hand, the search range of correspondences increases, and in turn, it increases the chances of false matching. The estimated disparity map is plausible in terms of depth, but it includes many small regions without depth as spatial artifacts (of holes) on the depth map. This missing information is caused by occlusion and false matching in featureless or pattern-repeated regions, where the corresponding point search fails.

Narrow-baseline stereo has a relatively short search range of correspondence. The search range of correspondence is shorter than that of wide-baseline stereo. There are fewer chances for false matching, so accuracy and efficiency in cost computation can be enhanced. In addition, the level of spatial noise in the disparity map is low because the occluded area is small. However, narrow-baseline stereo reserves a small number of pixels for depth discrimination. The depth-discriminative power decreases accordingly, whereas the spatial artifacts in the disparity map are reduced. It trades off the discriminative power for the reduced spatial artifacts in the disparity map.

2.1.1. Multi-baseline stereo approaches

This fundamental limitation of the baseline in binocular stereo has been addressed by the use of more than two cameras, so-called multi-baseline or multi-view stereo. Okutomi and Kanade [6] proposed a multi-baseline stereo method, which is a variant of multi-view stereo. The proposed system consists of multiple cameras on a rail. They presented the matching cost design for the multi-baseline setup. Instead of computing the color difference of a pixel on the reference view and the corresponding point on the other view, the color differences of all views are summed up. This multi-baseline stereo gives more accurate depth estimates than binocular stereo does.

Furukawa and Ponce [13] presented a hybrid patch-based multi-view stereo algorithm that is applicable to objects, scenes, and crowded scene data. Their method produces a set of small patches from matched features, which allows the gaps between neighboring feature points to be filled in, yielding a fine mesh model. Gallup et al. [14] estimated the depth of a scene by adjusting the baseline and the resolutions of images from multiple cameras so

that depth estimation becomes computationally efficient. This system exploits the advantages of multi-baseline stereo while requiring the mechanical support of moving cameras. Nakabo et al. [11] presented a variable-baseline stereo system on a linear slider. They controlled the baseline of the stereo system in relation to the target scene to estimate the accurate depth map.

Zilly et al. [7] introduced a multi-baseline stereo system with various baselines. Four cameras are configured in multiple baselines on a rail. The two inner cameras establish a narrow-baseline stereo pair while two outer cameras form a wide-baseline stereo pair. They then merge depth maps from two different baselines. The camera viewpoints in the multi-baseline systems are secured mechanically at fixed locations in general. This design restricts the spatial resolution along the camera array while the depth map is being reconstructed. Refer to [15] for the in-depth investigation of other multi-view methods.

Compared to the previous multi-baseline systems, we utilize a refractive medium on a rotary stage that is installed ahead of one of the binocular cameras. Our system requires only two cameras for binocular stereo, which is more efficient than other multi-baseline systems [7] that employ more than two cameras. In multi-baseline systems [11], it is cumbersome to move a camera along a linear slider. This manual operation may suffer from misregistration and broken calibration of multiview images, and such systems require a large space to operate for the camera movement. In the proposed system, we simply rotate a medium, instead of a camera, and can avoid any problems caused by the change of camera position. The form factor of our system is much smaller than that of multi-baseline systems [7,11].

2.2. Refractive stereo

Refractive stereo estimates depth using the refraction of light via a transparent medium. We follow the derivation of Gao and Ahuja [9] to formulate the optical geometry in refractive stereo. Suppose point p in a three-dimensional scene is projected to p_d on an image plane through the optical center of an objective lens C directly without any transparent medium (see Fig. 2a). Insertion of a transparent medium in the light path changes the transport of the incident beam from p, and it reaches p_r on the image plane with a lateral displacement d (between with and without the medium). The displacement between p_d and p_r on the image plane is called *refractive disparity*.

Now we can compute the depth z of p using simple trigonometry following [8,9]:

$$z = f\frac{R}{r}, \tag{2}$$

where r is a refractive disparity completed by searching a pair of corresponding points, f is the focal length, and R is the ratio of lateral displacement d to $\sin(\theta_p)$:

$$R = \frac{d}{\sin(\theta_p)}. \tag{3}$$

Here θ_p is the angle between $\overrightarrow{p_rC}$ and the image plane. To obtain the value of R, we first compute $\cos(\theta_p)$ as

$$\cos(\theta_p) = \frac{\overrightarrow{p_re} \cdot \overrightarrow{p_rC}}{\left|\overrightarrow{p_re}\right|\left|\overrightarrow{p_rC}\right|}. \tag{4}$$

Then we plug $\sin(\theta_p)$ into Eq. (3) after computing $\sin(\theta_p)$ with this equation:

$$\sin^2(\theta_p) + \cos^2(\theta_p) = 1. \tag{5}$$

Lateral displacement d, the parallel-shifted length of the light passing through the medium, is determined as [16]

$$d = \left(1 - \sqrt{\frac{1-\sin^2(\theta_i)}{n^2-\sin^2(\theta_i)}}\right) t\sin(\theta_i), \tag{6}$$

where t is the thickness of the medium, n is the refractive index of the medium, and θ_i is the incident angle of the light. Here, $\sin(\theta_i)$ can be obtained in a similar manner as the case of $\sin(\theta_p)$ using the following equation:

$$\cos(\theta_i) = \frac{\overrightarrow{p_rC} \cdot \overrightarrow{eC}}{\left|\overrightarrow{p_rC}\right|\left|\overrightarrow{eC}\right|}. \tag{7}$$

The refracted point p_r lies on a line, the so-called *essential line*, passing through *essential point* e (an intersecting point of the normal vector of the transparent medium to the image plane) and p_d (see Fig. 2b). This property can be utilized to narrow down the search range of correspondences onto the essential line, allowing us to compute matching costs efficiently. It is worth noting that disparity in refractive stereo depends on not only the depth z of p but also the projection position p_d of light and the position of the essential point e, whereas disparity in traditional stereo depends on only the depth z of the point p. Before estimating a depth, we calibrate these optical properties in refractive stereo in advance.

2.2.1. Refractive stereo approaches

Nishimoto and Shirai [17] first introduced a refractive camera system in which a refractive medium is placed in front of a camera. Rather than computing depth from refraction, their method estimates depth using a pair of a direct image and a refracted one, assuming that the refracted image is equivalent to one of the binocular stereo images. Lee and Kweon [18] presented a single camera system that captures a stereo pair with a bi-prism. The bi-prism is installed in front of the objective lens to separate the input image

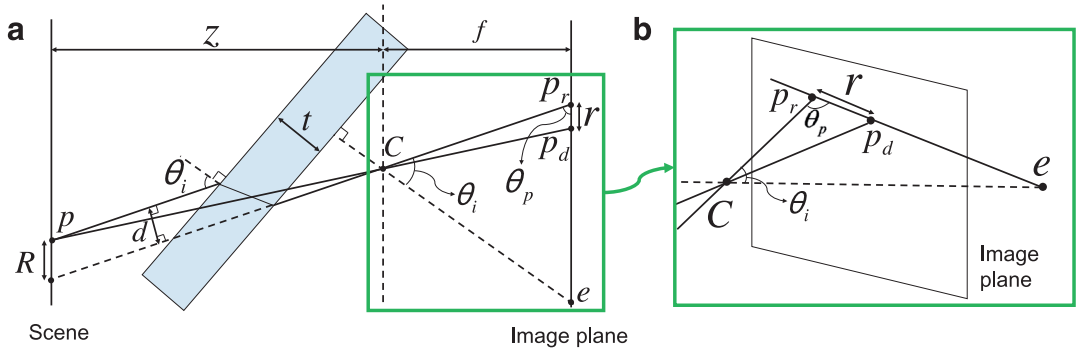

Fig. 2. (a) Cross-section view of the light path in refractive stereo. (b) Close-up view of refractive light transport in 3D.

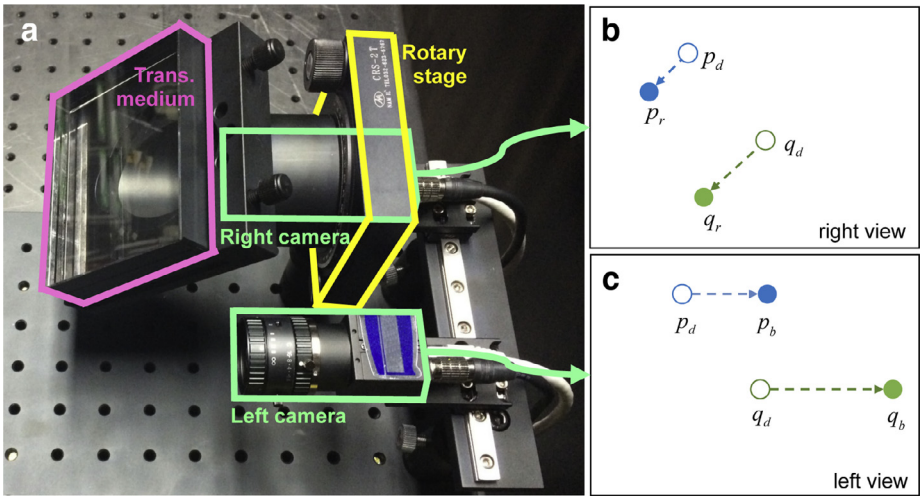

Fig. 3. (a) Our system prototype. (b) Point p is farther from the camera than point q. If there were no transparent medium in front of the right camera, points p and q are projected at pixels p_d and q_d via perspective projection. As the rays are refracted by the transparent medium, they are projected into p_r and q_r with the offsets of refractive disparities, which depend on the pose of the medium and the depths of p and q. (c) The left camera is installed next to the right camera with a baseline. Owing to parallax, the corresponding points are projected to p_b and q_b with binocular disparity. Note that these offsets are larger than p_r and q_r.

into a stereo pair with refractive shift. The captured image includes a stereo image pair with a baseline. Depth estimation is analogous to the traditional methods. Gao and Ahuja [8,9] proposed a seminal refractive stereo method that captures multiple refractive images with a glass medium tilted at different angles. This method requires the optical calibration of every pose of the medium. It was extended by placing a glass medium on a rotary stage in [9]. The rotation axis of the tilted medium is mechanically aligned to the optical axis of the camera. Although the mechanical alignment is cumbersome, this method achieves more accurate depth than the previous one does.

Shimizu and Okutomi [19,20] introduced a mixed approach that combines refraction and reflection phenomena. This method superposes a pair of reflection and refraction images via the surface of a transparent medium. These overlapping images are utilized as a pair of stereo images. Chen et al. [10,21] proposed a calibration method for refractive stereo. This method finds the pairs of matching points on refractive images with the SIFT algorithm [22] to estimate the pose of a transparent medium. They then search corresponding features using the SIFT flow [23]. By estimating the rough scene depth, they recover the refractive index of a transparent medium.

3. System implementation

We propose a novel stereo fusion system that exploits the advantages of refractive and binocular stereo. This section describes technical details of the hardware design and calibration methods for the proposed system.

3.1. Hardware design

Our stereo fusion system consists of two cameras and a transparent medium on a mechanical support structure. The focal length of both camera lenses is 8 mm. The cameras are placed on a rail in parallel with a baseline of 10 cm to configure binocular stereo. We place a transparent medium on a rotary stage for refractive stereo in front of one of the binocular stereo cameras. Fig. 3(a) presents our system prototype. Fig. 3(b) and (c) compare disparity changes by the refractive medium (b) and the baseline in stereo (c), respectively. Suppose we have two points, p and $q \in \mathbb{R}^3$, where point p is farther from the camera than point q. In Fig. 3(b), if there is no transparent medium, points p and q will be projected at pixels p_d and q_d via perspective projection, respectively. However, as we have the medium, rays are refracted and projected at pixels p_r and q_r due to refraction caused by the medium. Note that the refractive disparity (the offset distance) depends on the depth of point, i.e., the refractive disparity of distant point p is shorter than that of q, and the orientation of refractive disparity depends on the pose of the medium. In Fig. 3(c), the left camera is installed next to the right camera with a baseline. The corresponding pixels p_d and q_d are projected on p_b and q_b with binocular disparities. Comparing the refractive and the binocular disparity, the refractive disparities p_r and q_r are smaller than those of binocular disparities p_b and q_b. Refractive stereo is equivalent to narrow-baseline stereo while binocular stereo is equivalent to wide-baseline stereo in our system.

Our transparent medium is a block of clear glass. The measured refractive index of the medium is 1.41 ($\eta = \sin(20.00^\circ)/\sin(14.04^\circ)$), and the thickness of the medium is 28 mm. We built a customized cylinder to hold the medium, cut in 45° from the axis of the cylinder. The tilted medium spins around the optical axis from 0° to 360° with angle intervals while capturing images. The binocular stereo baseline and the tilted angle of the medium are fixed rigidly during image capturing. For the input images of a scene, multiple images refracted by the medium are captured on a camera and another image is obtained from the other camera without the glass. Note that the refractive medium is not detached while capturing the input.

3.2. Calibration

Our stereo fusion system requires several stages of prior calibration to estimate depth information. This section summarizes our calibration processes.

3.2.1. Geometric calibration

We first calibrate the extrinsic/intrinsic parameters of the cameras, including the focal length of the objective lens, the center point of the image plane and the lens distortion in order to convert the image coordinates into the global coordinates. For the geometric calibration, we captured 14 different positions on a chessboard. This allows us to derive an affine relationship between the two cameras and rectify the coordinates of these cameras with respect to the constraint epipolar line [24].

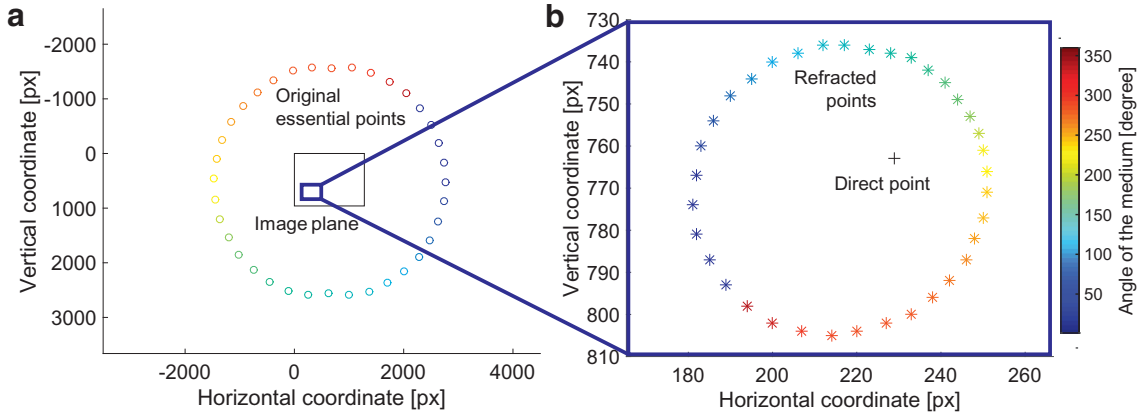

Fig. 4. (a) Presents the calibrated results of 36 essential points measured by Baek and Kim's method [12]. (b) shows the locations of 36 refracted points from a direct point in the coordinates of (763,229) at a distance of 40 cm. This figure shows that the direct point is refracted to 36 different positions depending on the medium orientation.

3.2.2. Refractive calibration

Refractive stereo demands several optical calibrations related with the glass medium, such as thickness, its refractive index, and the essential points of glass orientation. This section presents our novel calibration method for refractive stereo.

Analogous to the rectification of the epipolar line in binocular stereo, refractive stereo requires calibration of the essential point e, where essential lines converge to the essential point e outside the image plane (see Section 2.2 for details on essential points and lines); i.e., the refracted point p_r passes through the virtually unrefracted pixel p_d and reaches the essential point e on the essential line (see Fig. 2b).

Gao and Ahuja [8,9] estimate essential points by solving an optimization problem with a calibration target at a known distance. They precompute the positions of the essential points at the entire angles by mechanically changing the normal orientation of the glass to each angle. Chen et al. [10] estimate essential points directly from a target scene without pre-calibration of essential points. Instead of capturing the calibration targets, they capture a target scene with and without the glass medium and apply the SIFT algorithm [10] to search correspondences of the refracted and unrefracted points. Their calibration process is simpler than that of previous works [8,9]. However, the accuracy of the calibration depends on the SIFT performance in searching correspondences.

Recently, Baek and Kim [12] calibrate essential points through dense measurements of essential lines at each medium orientation using a calibration target. They take an image of a chessboard without the medium first in order to compare it with other refracted images at different poses of the medium. Once they take a refracted image in a pose, they extract corner points from both the direct and the refracted images, where corresponding feature points appear at different positions due to refraction. Superposing these two images, they draw lines by connecting the corresponding points with all feature corners following Chen et al. [10]. They then compute the arithmetic mean of the intersection points' coordinates to approximate essential point e_ϕ per angle ϕ. They repeat this process for every angle $\phi \in \Phi$, where Φ is the set of angles for calibration. Fig. 4(a) presents the calibrated essential points for Φ measured from 36 different orientations.

Whereas Gao and Ahuja [8,9] require the measurement between the target and the camera in addition to measuring essential lines, the method proposed by Baek and Kim [12] does not require measurement of the distance from the camera to the chessboard, and thus is more convenient. Note that Gao and Ahuja [9] should capture four angles of the medium iteratively, until the rotation axis of the medium meets the principal axis of the camera. Contrary to Chen et al. [10], Baek and Kim [12] employ a calibration target to enhance the reliability of refractive calibration. However, since their calibration requires rigorous measurements of the entire angle variation, their measurement step in refractive calibration is very cumbersome and introduces any measurement errors.

In order to overcome the problem of cumbersome measurements in the calibration process, we propose a modified approach of the previous refractive calibration introduced by Baek and Kim [12]. We were motivated to reduce the number of per-angle measurements of correspondences while estimating the entire essential points.

Euler angle-based calibration. We propose a novel parametric approach of refractive calibration on essential points. The key idea is to approximate the entire essential points of every angle by using a parametric rotation of xyz-Euler angles, where the rotation axis vector is optimized from a subset of measured essential points.

Suppose we already estimated a certain number of essential points e_ϕ for sampled angles $\phi \in \Phi$ following Baek and Kim [12]. Let the rotation axis of the medium be a unit vector $\mathbf{u} = [u_x, u_y, u_z]^\intercal$, where $\|\mathbf{u}\|_2 = 1$. We denote the unit normal vector of the medium at angle φ as $\mathbf{n}(\varphi) = [n_x(\varphi), n_y(\varphi), n_z(\varphi)]^\intercal$, where $\|\mathbf{n}(\varphi)\|_2 = 1$. Without loss of generality, we set the reference angle (one of the measured angles) as zero degree. When we rotate the medium by degree φ from the reference angle with respect to the rotation axis $\mathbf{u}$, the corresponding normal vector $\mathbf{n}(\varphi)$ of the medium can be computed as follows:

$$\mathbf{n}(\varphi) = T(\varphi, \mathbf{u})\mathbf{n}(0), \tag{8}$$

where $T(\varphi, \mathbf{u})$ is a rotation matrix that rotates a given vector $\mathbf{n}(0)$ by degree φ with respect to $\mathbf{u}$. $T(\varphi, \mathbf{u})$ is defined as an xyz-Euler angle rotation matrix with a rotation axis $\mathbf{u}$ following [25]:

$$T(\varphi, \mathbf{u}) = \begin{bmatrix} u_x^2 v + c & u_x u_y v - u_z s & u_x u_z v + u_y s \\ u_y u_x v + u_z s & u_y^2 v + c & u_y u_z v - u_x s \\ u_z u_x v - u_y s & u_z u_y v + u_x s & u_z^2 v + c \end{bmatrix}, \tag{9}$$

where c is defined as $cos\varphi$, s is $sin\varphi$, and $v := 1 - c$.

Let e_φ be the essential point for a pose of the medium, rotated about degree φ from the reference pose with respect to $\mathbf{u}$. The essential point e_φ in the image plane is located on a line that passes through the center of optics C. By definition, the unit normal vector of the medium $\mathbf{n}(\varphi)$ is on the same line (see Fig. 5). We then formulate this relation between the essential point e_φ and the

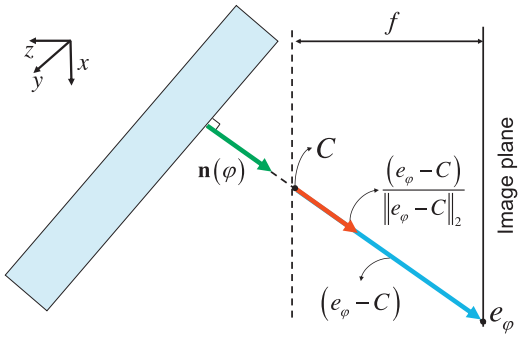

Fig. 5. For angle φ of the medium, essential point e_φ is formed as an intersection point in the image plane on a line that passes through the center of optics C. The unit normal vector of the medium $\mathbf{n}(\varphi)$ is on the same line.

normal $\mathbf{n}(\varphi)$ as follows:

$$\mathbf{n}(\varphi) = \frac{e_\varphi - C}{\|e_\varphi - C\|_2}. \tag{10}$$

We denote the right-hand side in Eq. (10), $(e_\phi - C)/\|e_\phi - C\|_2$, as K_ϕ. Our goal is to formulate essential points from any given angle rotation as a parametric calibration model. This axis vector $\mathbf{u}$ and the reference normal $\hat{\mathbf{n}}(0)$ satisfy Eqs. (8) and (10) from known values K_ϕ and can be formulated as an objective function:

$$\min_{\mathbf{u},\hat{\mathbf{n}}(0)} \sum_{\phi\in\Phi} \|T(\phi,\mathbf{u})\hat{\mathbf{n}}(0) - K_\phi\|_2 \quad \text{s.t.} \|\hat{\mathbf{n}}(0)\|_2 = 1 \text{and} \|\mathbf{u}\|_2 = 1, \tag{11}$$

where $\hat{\mathbf{n}}(0)$ is the optimized reference normal of the medium. Note that it is feasible to use $\mathbf{n}(0)$ directly instead of introducing $\hat{\mathbf{n}}(0)$ using Eq. (10). However, we found that when one of direct measured normals is used as $\mathbf{n}(0)$ in optimization of Eq. (11), optimized essential points can be biased occasionally upon an initial measurement error of $\mathbf{n}(0)$. We therefore choose to apply a joint optimization approach to find both optimal $\hat{\mathbf{n}}(0)$ and $\mathbf{u}$ in order to enhance global accuracy.

We solve this non-linear objective function using a non-linear optimization algorithm [26]. Note that we have six unknown variables of $\mathbf{u}$ and $\hat{\mathbf{n}}(0)$. Since the *unit* normal vector $\mathbf{n}(\varphi)$ has rank 2, Eq. (11) gives us two equations per angle ϕ. Therefore, we need at least three samples to solve Eq. (11). See Fig. 12 for the impact of the number of input angles.

After optimizing $\mathbf{u}$, we can compute the essential point e_φ at any arbitrary angle φ of the medium. The essential point e_φ is the intersection point of a line that passes through the center of optic C displaced with f along the $-z$ axis (see Fig. 5). Therefore, we can compute the essential point e_φ as follows:

$$e_\varphi = \frac{T(\varphi,\mathbf{u})\hat{\mathbf{n}}(0)}{-T_z(\varphi,\mathbf{u})\hat{\mathbf{n}}(0)} f + C, \tag{12}$$

where $T_z(\varphi, \mathbf{u})$ is the z-axis vector of $T(\varphi, \mathbf{u})$.

In our experiment, we select a set of angles Θ to be used to estimate corresponding essential points from the estimated $\mathbf{u}$ with Eq. (8). We denote the set of essential points as E for depth estimation.

3.2.3. Radiometric calibration

Matching costs are calculated by comparing the intrinsic properties of color at feature points. Since we attach a transparent medium on one of the stereo cameras, it is critical to achieve consistent camera responses with and without the medium. In our system, the right camera is attached with the glass medium while the left camera is without any medium. We found that there are mismatches of colors captured in the same scene. We therefore characterize these two cameras via radiometric calibration to match colors with each other. To do this, we employed a Gretag-Macbeth ColorChecker target of 24 color patches. We first captured an image from the refractive module with the medium and an image from the other camera without the medium. Then, we linearized these two RGB images with known gamma values as inverse gamma correction. Since we had two sets of the linear RGB colors for the 24 patches, A and B (with and without the medium), of which the dimensions were 24 × 3 each, we determined an affine transformation M of A to B as a camera calibration function (a 3 × 3 matrix) using least-squares [27]. Once we characterized two camera responses, we applied this color transform M for the linear RGB image which was reconstructed from the images taken by the camera with the medium (see Section 4.1.3). This color characterization allowed us to evaluate matching costs for disparity through identical color reproductions of the two different cameras.

4. Depth reconstruction in stereo fusion

Our stereo fusion workflow is composed of two stages. We first estimate an intermediate depth map from a set of refractive stereo images (from the camera with the refractive medium) and reconstruct a synthetic direct image. Then, this virtual image and a direct image (from the other camera without the medium in a baseline) are used to estimate the final depth map referring to the intermediate depth map from refractive stereo. Fig. 6 presents the workflow of our stereo fusion method.

4.1. Depth from refraction

Depth reconstruction from binocular stereo has been well-studied regarding matching cost computation, cost aggregation, disparity computation, and disparity refinement [1], whereas depth reconstruction from refraction has been relatively less discussed. In this section, we describe our approach for refractive stereo for reconstructing an initial depth map.

4.1.1. Matching cost in refractive stereo

Binocular stereo algorithms often define the *matching cost volumes* of every pixel per disparity [1], where a disparity value indicates a certain depth distance directly in binocular stereo. This linear relationship can be universally applied for all the pixels in stereo images. However, it is worth noting that the refractive disparity of a pixel depends on not only depth but also on its image coordinates and the pose of the medium in refractive stereo; i.e., the refractive disparities of a point on the object's surface could be different when the pixel position or the pose of the medium is different. We therefore define the matching cost volumes based on the depth, rather than the disparity, in our refractive stereo algorithm, following a plane sweeping stereo method [28]. This approach allows us to apply a cost volume approach for refractive stereo.

Suppose we have a geometric position set P of the refracted points $p_r(p_d, z, e)$ of direct point p_d at depth z (see Fig. 2) with essential point e ($e \in E$):

$$P(p_d, z) = \{p_r(p_d, z, e) | e \in E\}. \tag{13}$$

This set P can be derived analytically by refractive calibration (Section 3.2.2) so that we precompute this set P for computational efficiency.

We denote L as the set of colors observed at the refracted positions P, where l is a color vector in a linear RGB color space

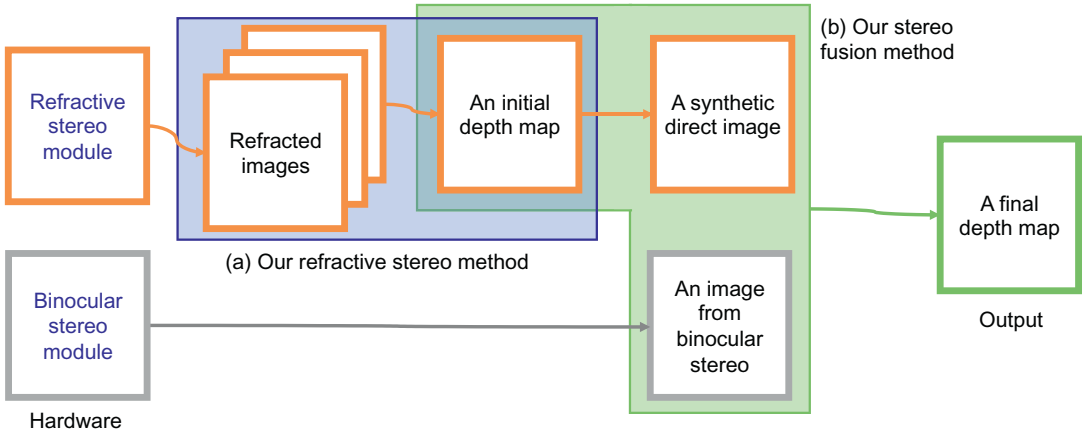

Fig. 6. Schematic diagram of our stereo fusion method. (a) Our refractive stereo method estimates an intermediate depth map from refractive stereo. (b) Our stereo fusion method reconstructs a final depth map from a pair of an image from binocular stereo and a synthetic direct image obtained using the intermediate depth map.

($l \in L$). Assuming that the surface of the direct point p_d is Lambertian, the colors of the refracted points $L(p_d, z)$ would be the same. We use the similarity of $L(p_d, z)$ for the matching cost C of p_d with hypothetical depth z [29]. Note that our definition of *the matching cost* is proportional to the similarity, different from the typical definition of the matching cost in traditional stereo algorithms. The definition of the matching cost is as follows:

$$C(p_d, z) = \frac{1}{|L(p_d, z)|} \sum_{l \in L(p_d, z)} K(l - \bar{l}). \tag{14}$$

K is an Epanechnikov kernel [30] following:

$$K(l) = \begin{cases} 1 - \|l/h\|^2, & \|l/h\| \le 1 \\ 0, & \text{otherwise} \end{cases}, \tag{15}$$

where h is a normalization constant ($h = 0.01$). Here, $\bar{l}$ is a mean color vector of all elements in a set of L. We compute $\bar{l}$ with five iterations in $L(p_d, z)$ using the mean shift method [31] as follows:

$$\bar{l} = \frac{\sum_{l \in L(p_d, z)} K(l - \bar{l}) l}{\sum_{l \in L(p_d, z)} K(l - \bar{l})}. \tag{16}$$

z in our refractive stereo is a discrete depth, the range of which is set between 60 cm and 120 cm at 3 cm intervals. Note that we build a refractive cost volume per depth for all the pixels in the refractive image.

4.1.2. Cost aggregation for depth estimation

To improve the spatial resolution of the intermediate depth map in refractive stereo, we aggregate the refractive matching cost using a window kernel G.

Advanced cost aggregation techniques, such as guided image [32] and bilateral weights [33], require a prior knowledge of the scene, i.e., a unrefracted direct image. However, we do not capture the direct image in our experiments because this requires detachment of the medium for every scene. Therefore, we first aggregate the refractive matching costs using a Gaussian kernel G:

$$G(p_d, q_d) = \frac{1}{2\pi\sigma^2} \exp\left(\frac{-||p_d - q_d||^2}{2\sigma^2}\right), \tag{17}$$

where σ is set to 9.6 as a parameter.

We filter the refractive matching cost at a pixel p_d in a depth z, where this kernel convolves $C(p_d, z)$ with the matching costs of neighboring pixels with a weighting factor $G(p_d, q_d)$ [34]:

$$C^A(p_d, z) = \sum_{q_d \in w} G(p_d, q_d) C(q_d, z), \tag{18}$$

where q_d is a pixel inside a squared window w, the size of which is 7×7.

Finally, we compute the optimal depth $Z(p_d)$ of the point p_d that maximizes the aggregated matching costs:

$$Z(p_d) = \arg\max_z C^A(p_d, z). \tag{19}$$

4.1.3. Reconstructing a synthetic direct image

Even though the levels of the two cameras are the same on a rail as traditional binocular stereo, our stereo pair includes more than horizontal parallax due to the refraction effect. Prior to combining the estimated refractive depth and the binocular stereo input, we reconstruct a synthetic image I_d (a direct image without the medium) by computing the mean radiance of the set $L(p_d, Z(p_d))$ using the mean shift method (Eq. (16)). Note that this set L consists of colors gathered from the refracted images.

Fig. 7 presents the initial depth map Z (a) and the reconstructed synthetic direct image I_d (d), which is compared with a ground truth image (e) that was captured while the medium was detached. If the refractive depth estimates $Z(p_d)$ contains some errors, the resulting synthetic image I_d also contains errors.

4.1.4. Depth and direct image refinement

Reconstructing the direct image allows us to apply a depth refinement algorithm with a weighted median filter [35] by treating the synthetic direct image as guidance to fill in the holes of the estimated depth map. The weighted median filter replaces the depth $Z(p_d)$ using the median from the histogram $h(p_d, \cdot)$:

$$h(p_d, z) = \sum_{q_d \in w} W(p_d, q_d) f(q_d, z), \tag{20}$$

where $f(q_d, z)$ is defined as follows:

$$f(q_d, z) = \begin{cases} 1, & \text{if } Z(q_d) - z = 0 \\ 0, & \text{otherwise} \end{cases}. \tag{21}$$

Here, W is a weight function with a guided image filter [32], defined as

$$W(p_d, q_d) = \frac{1}{|w|^2} \sum_{k:(p_d, q_d) \in w_k} (1 + (I_d(p_d) - \mu_k)(\Sigma_k + \epsilon U)^{-1} (I_d(q_d) - \mu_k)), \tag{22}$$

where $I_d(p_d)$ is the linear RGB color of p_d on the direct image I_d, U is an identity matrix, k is the center pixel of window w_k including p_d and q_d, $|w|$ is the number of pixels in w_k, and μ_k and Σ_k are

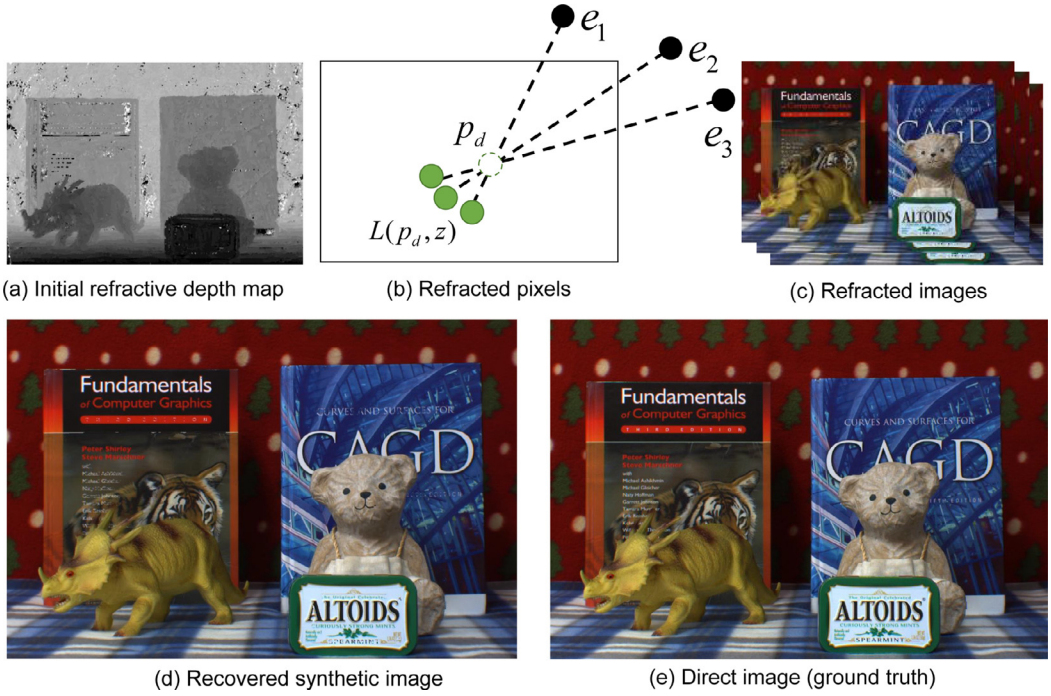

Fig. 7. (a) Shows an initial depth map. (b) shows the the computed positions of refracted pixels corresponding to the three essential points using the depth estimates (a). We recover a synthetic direct image (d) by computing the arithmetic mean of the corresponding refracted pixel colors (b) on the refracted images (c). (d) and (e) compare the synthetic image with a ground truth image that was captured while the medium was detached.

the mean vector and covariance matrix of I_d in w_k. In our experiments, we set the size of w_k as 9×9, and we set ϵ as 0.001.

This median filter allows us to refine the hole artifacts in the depth map while preserving sound depth. Once we obtained this refined depth map, we iteratively build a synthetic image again using the refined depth map. Fig. 8 compares the initial synthetic image and the refined synthetic image from the second iteration.

We next complete the synthetic direct image from the refracted images to be used as the input of binocular stereo. Since these two cameras' color reproductions are different due to the insertion of the glass medium, we apply the color calibration matrix (described in Section 3.2) to the synthetic image.

4.2. Number of refractive images

The number of input refractive images is critical to the quality of depth estimation in refractive stereo. We were motivated to identify the effects of number of input refractive images; therefore, we evaluated point-wise errors in estimating the depth on a planar surface at a known distance. We computed the root-mean-square error (RMSE) of depth estimates on a planar surface, indicated as a red rectangle in Fig. 9(a). Fig. 9(b) shows that the RMSE decreased very fast, while the input increased to six refractive images. Hence, we determined that we could utilize six refractive images as input considering the tradeoff between computation cost and depth

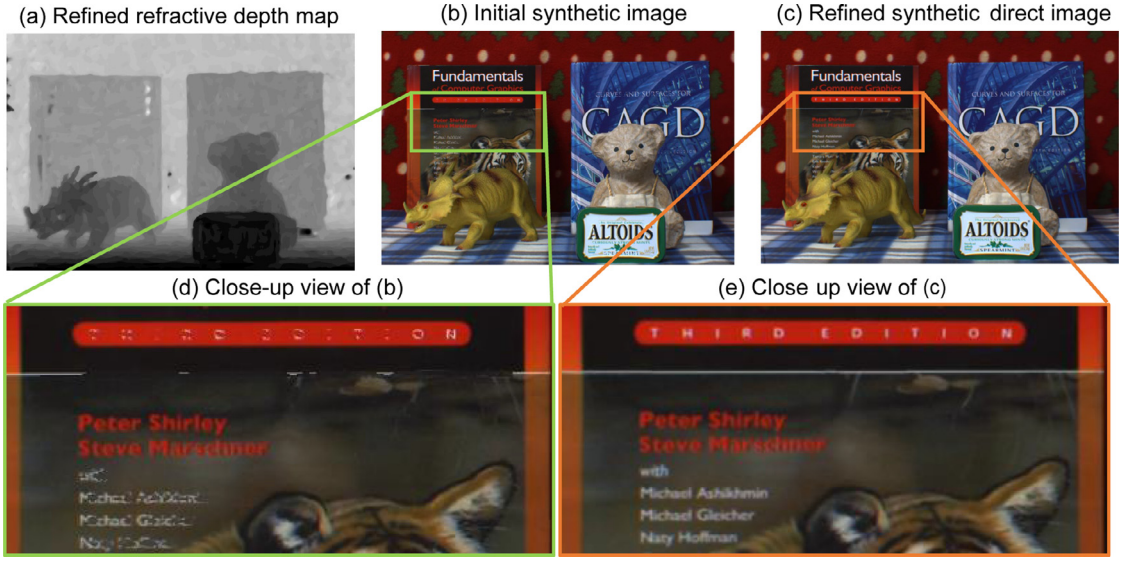

Fig. 8. (a) Shows the refined depth map with weighted median filtering [35]. A synthetic direct image (c) is computed again using the refined depth map (a), used for binocular stereo later. (b) is the initial synthetic image. The refined synthetic image (e) has more details than the initial synthetic image (d).

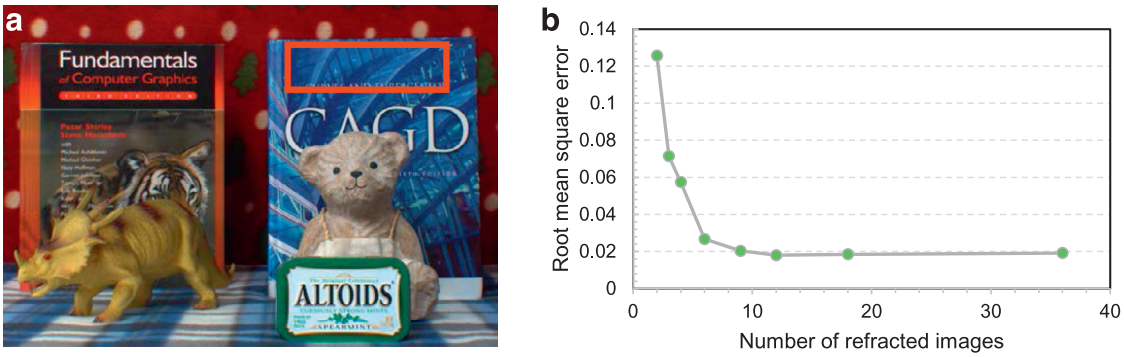

Fig. 9. (a) The red square indicates the area used for finding effects of number of input refractive images for depth accuracy. The book cover is a planar surface orthogonal to the camera optical axis with a constant depth. (b) The depth error quickly decreased significantly up to six refractive inputs with different angles. No significant improvement is observed with more than six inputs. (For interpretation of the references to color in this figure legend, the reader is referred to the web version of this article).

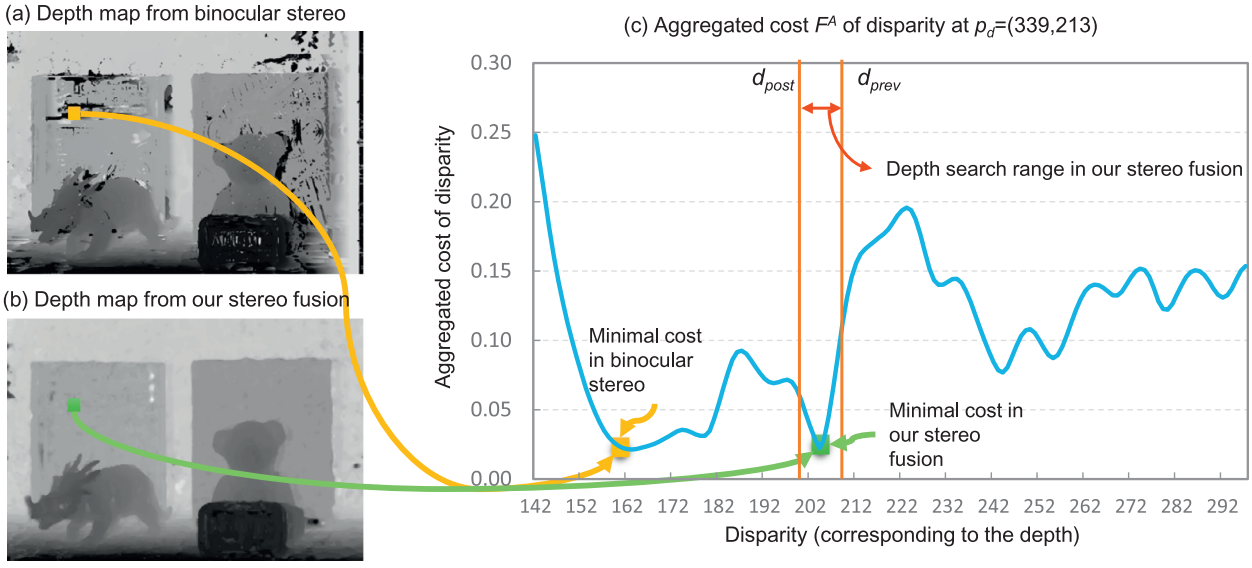

Fig. 10. The binocular depth map (a) includes artifacts due to false matching caused by occlusions, featureless regions and repeated patterns. Using the intermediate refractive depth map (b), we can limit the search range of a corresponding point p_d between d_{post} and d_{prev} for instance. This significantly reduces false matching frequency in estimating depth.

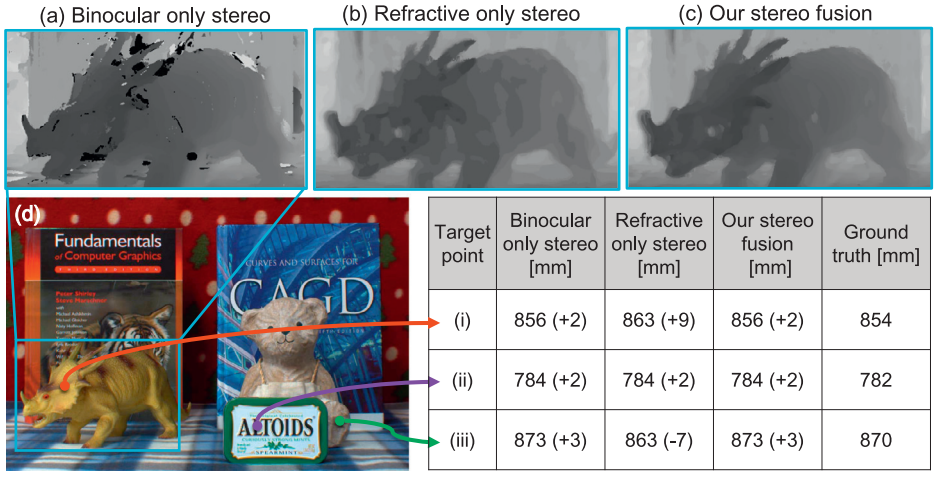

Target point	Binocular only stereo [mm]	Refractive only stereo [mm]	Our stereo fusion [mm]	Ground truth [mm]
(i)	856 (+2)	863 (+9)	856 (+2)	854
(ii)	784 (+2)	784 (+2)	784 (+2)	782
(iii)	873 (+3)	863 (-7)	873 (+3)	870

Fig. 11. The top rows compares the three different depth maps of binocular only stereo (a), refractive only stereo (b) from the intermediate stage of our fusion method and our stereo fusion (c) for a scene (d). Our stereo fusion method (c) does not suffer from false matchings occurring at binocular only stereo (a). The bottom-right table presents the measured depth values on three points in the scene, demonstrating that our method can discriminate close surfaces, such as (i) and (iii), as much as binocular stereo does. Note that refractive stereo cannot distinguish the depth differences between (i) and (iii).

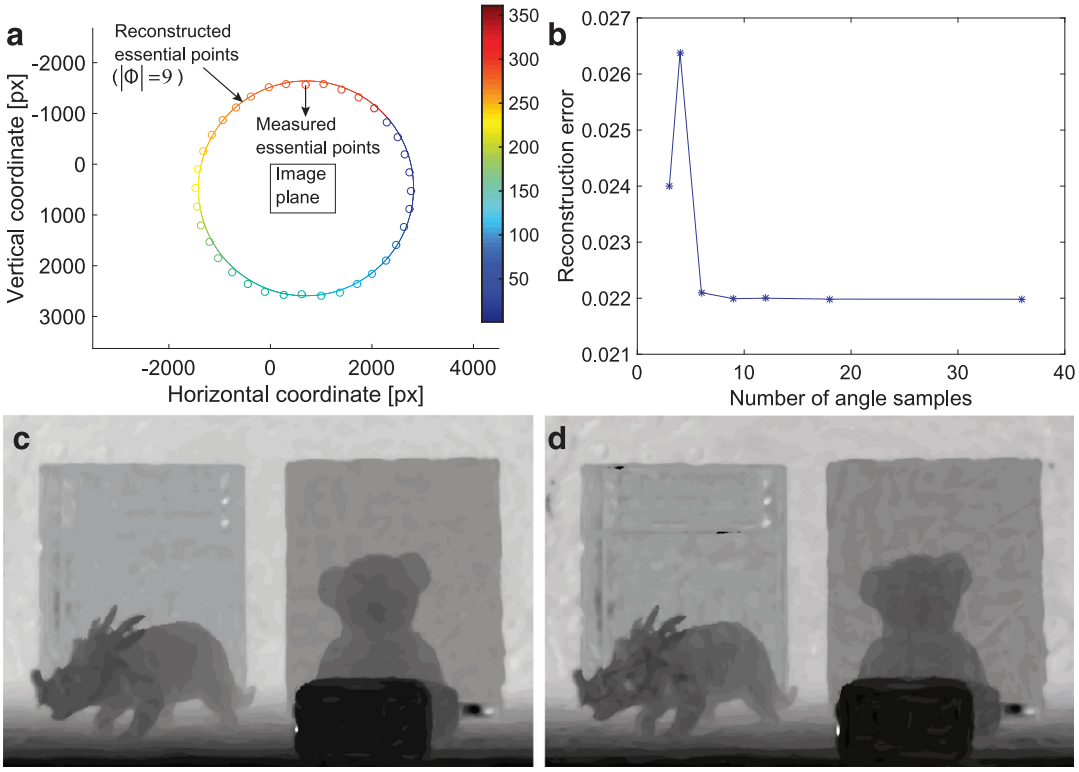

Fig. 12. (a) Shows the measured essential points (circles), and the essential points (solid line) calibrated from nine sampled angles. (b) describes the averaged calibration error of normals. The calibration error decreases rapidly up to nine sampled angles. We therefore chose nine angles for our calibration. (c) shows the refractive depth map obtained by 36 essential points measured. We reconstruct a plausible depth map (d), with 36 reconstructed essential points, obtained by nine sampled angles for calibration. Quantization artifacts shown in the depth maps will be handled by our stereo fusion stage.

accuracy. Note that we use six refractive images with 60° intervals for capturing results in this paper.

4.3. Depth in stereo fusion

Our binocular stereo with a wider baseline allows us to discriminate depth with a higher resolution than refractive stereo (equivalent to narrow-baseline stereo). We take inspiration from a coarse-to-fine stereo method [36,37] to develop our stereo fusion method. Our refractive stereo yields an intermediate depth map with a high spatial resolution that is on a par with that of narrow-baseline stereo. However, it is not surprising that the z-depth resolution of this depth map is discrete and coarse. We utilize the fine depth map from refractive stereo to increase the z-depth resolution as high as possible with a high spatial resolution by limiting the search range of matching cost computation in binocular stereo using the refractive depth map. To this end, we can significantly reduce the chances of false matching while estimating depth from binocular stereo between direct and synthetic images. This enables us to achieve a fine depth map from binocular stereo, taking advantages of a high spatial resolution in refractive stereo.

4.3.1. Matching cost in stereo fusion

Now we have a direct image I_b from the camera without the medium in the binocular module and the synthetic image I_d reconstructed from the refractive stereo module (Section 4.1.4) with its depth map. Depth candidates with uniform intervals are not related linearly to the disparities with pixel-based intervals. Hence, we define a cost volume for stereo fusion on the disparity instead in order to fully utilize the image resolution. To fuse the depth from binocular and refractive stereo, we build a fusion matching cost volume $F(p_d, d)$ per disparity for all pixels as follows. The fusion matching cost F is defined as a norm of the intensity difference:

$$F(p_d, d) = \left\| I_d(p_d) - I_b(p'_d) \right\|, \tag{23}$$

where p'_d is a pixel shifted by a disparity d from p_d, and $I_b(p'_d)$ is a color vector of p'_d on image I_b.

4.3.2. Cost aggregation in stereo fusion

In order to aggregate sparse matching costs, we first tried to use a guided image filter that consists of multiple box filters, as done when refining refractive depth. Prior to applying this filter, we reduce the search range of correspondence differently per each pixel using the depth map obtained from refractive stereo. Since the guided filter exploits integral images, which need to be constructed for every pixel and every depth candidate, its computational cost increases significantly due to the wide range of valid depth candidates for high depth resolution. Instead of the guided filter, we use a bilateral filter W in Eq. (24), as the filter can be applied to the different ranges of depths per pixel independently. We achieve a significant improvement in computational cost by applying the bilateral image filter within a narrowed search range using the depth prior from refractive stereo, while maintaining high depth resolution. The size of the kernel w is 9×9, and the value of ϵ is 0.001 in our experiments. The aggregated cost of the fusion matching costs in our method is defined as

$$F^A(p_d, d) = \sum_{q_d \in w} W(p_d, q_d) F(q_d, d). \tag{24}$$

Here W is the bilateral image filter [34] defined as

$$W(p_d, q_d) = exp\left\{ -\frac{d(p_d, q_d)}{\sigma_s^2} - \frac{c(p_d, q_d)}{\sigma_c^2} \right\}, \tag{25}$$

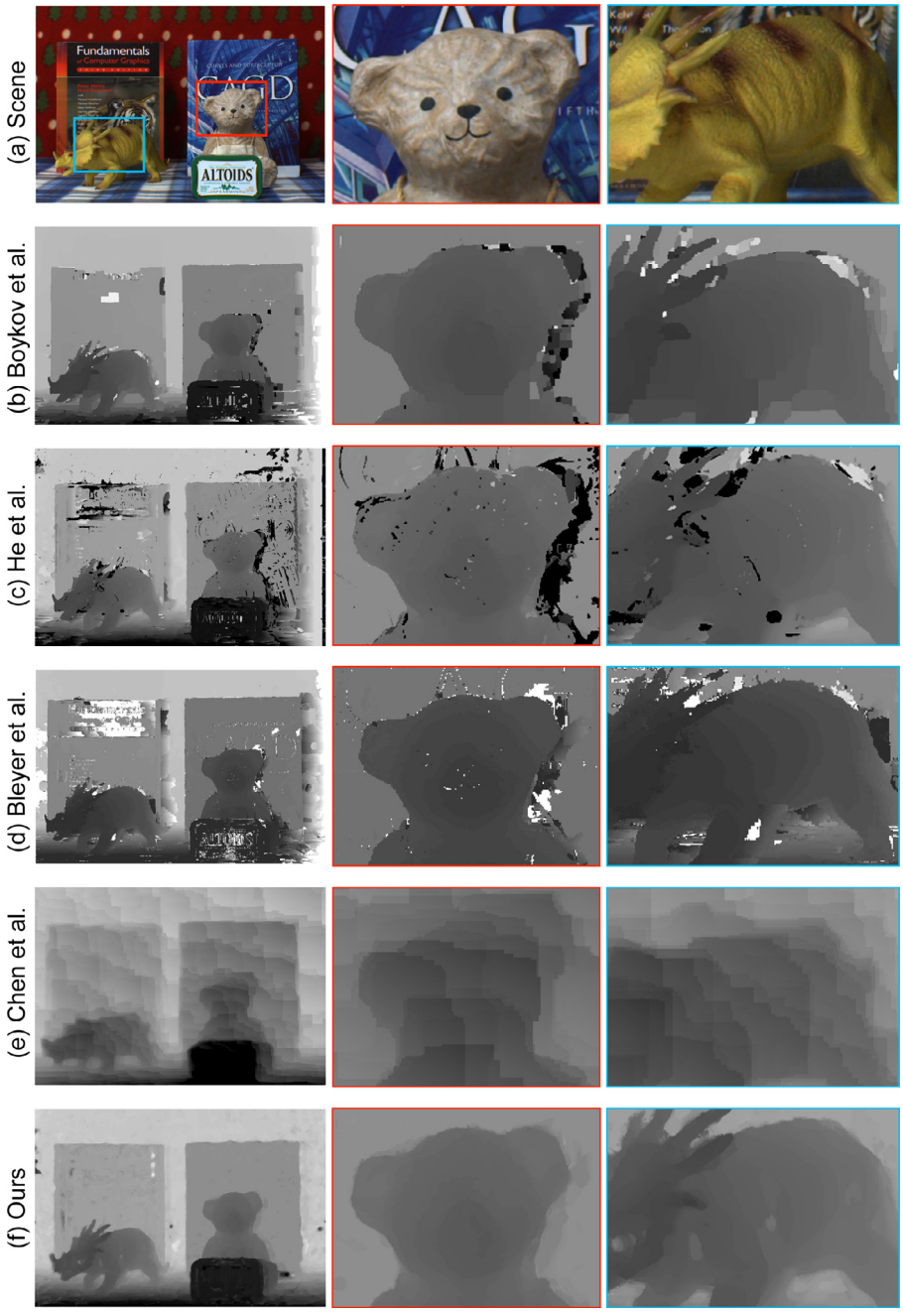

Fig. 13. Depth maps of a scene (a) are computed by five different methods. (b) and (c) show depth maps produced by global [38] and local binocular stereo [32] methods. (d) shows the depth maps obtained by a patchmatch-based binocular stereo method [39]. (e) presents depth maps produced by a refractive stereo method [10]. Our method (f) estimates depth accurately without suffering from severe artifacts.

where $d(p_d, q_d)$ is the Euclidean distance between p_d and q_d, $c(p_d, q_d)$ is the sum of differences of colors of RGB channels, and σ_s and σ_c are the standard deviations for spatial distance and color difference, respectively. In our experiment, we selected the window size, σ_s, and σ_c as 9, 7, and 0.07 respectively.

Suppose the depth of point p_d is estimated as $Z(p_d)$ from refractive stereo. As we compute the refractive matching cost and aggregate the cost *per discrete depth interval* Δz in refractive stereo, let the actual depth of p_d be between $(Z(p_d) - \Delta z)$ and $(Z(p_d) + \Delta z)$ as Z_{prev} and Z_{post}. The corresponding disparities of Z_{prev} and Z_{post} can be computed as d_{prev} and d_{post} using Eq. (1). Note that d_{post} is smaller than d_{prev}. We therefore estimate the optimal disparity $D(p_d)$ by searching the aggregated cost volume $F^A(p_d, d)$ within the range $[d_{post}, d_{prev}]$ as follows:

$$D(p_d) = \arg\min_d F^A(p_d, d). \tag{26}$$

Note that we compute Eq. (24) within the range of $[d_{post}, d_{prev}]$ exclusively for computational efficiency.

The ground true disparity of an orange pixel in Fig. 10(a) is approximately 200. However, the disparity from binocular stereo was estimated as 160 because the minimum aggregated cost of binocular disparity has a local minimum, yielding a wrong depth estimate. As a result, we were motivated to take a coarse-to-fine approach using both binocular and refractive disparity maps. As shown in Fig. 10(b), the refractive depth map tends to have fewer spatial artifacts. We use this refractive disparity map as a guide

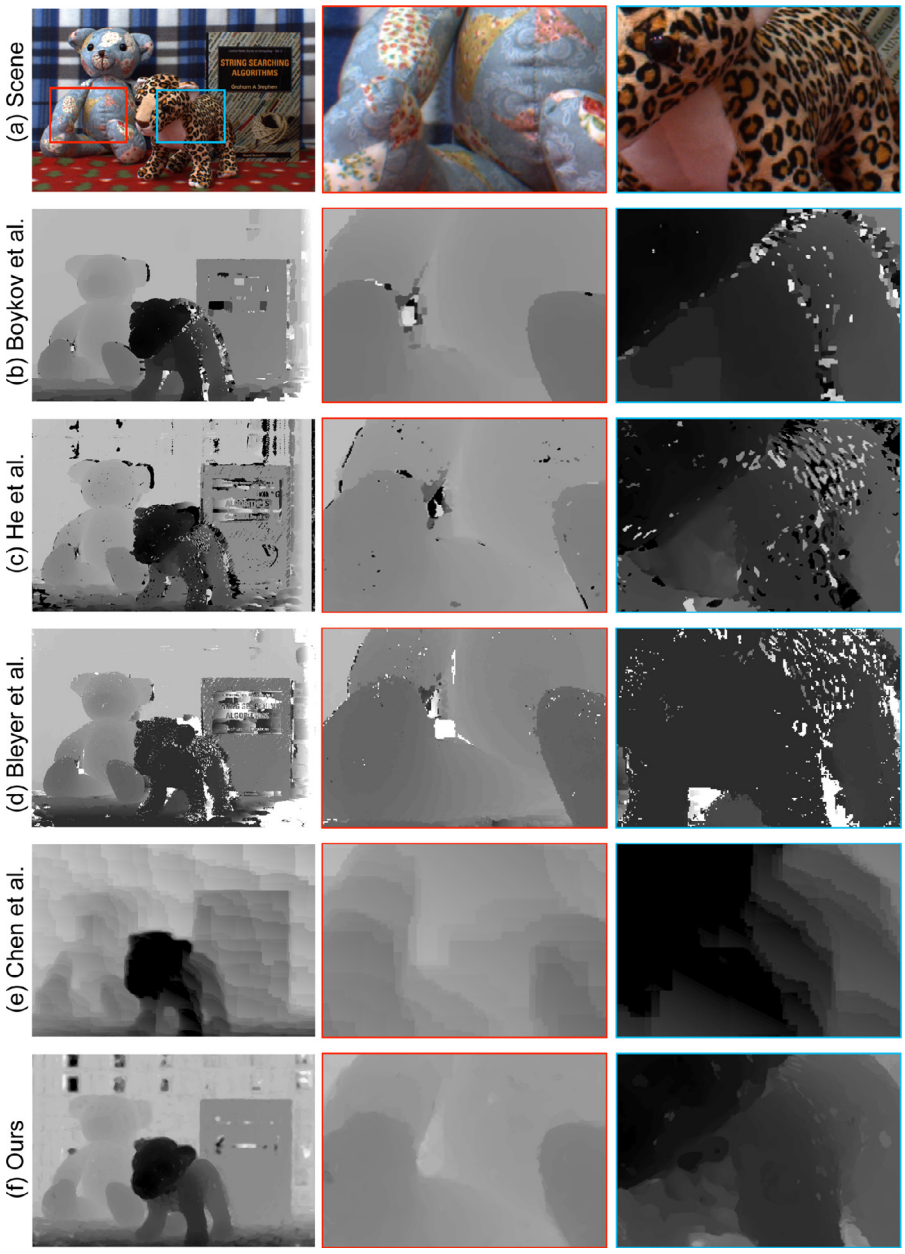

Fig. 14. Depth maps of a scene (a) are computed by five different methods. (b) and (c) show depth maps produced by global [38] and local binocular stereo [32] methods. (d) shows the depth maps obtained by a patchmatch-based binocular stereo method [39]. (e) presents depth maps produced by a refractive stereo method [10]. Our method (f) estimates depth accurately without suffering from severe artifacts.

map for searching aggregated disparities. The search range is set to $[d_{post}, d_{prev}]$ around the refractive depth estimate with a threshold. To this end, we are capable of preventing faulty estimates in our stereo fusion.

5. Results

5.1. Implementations

We conducted several experiments to evaluate the performance of our stereo fusion method. We computed depth maps, the resolution of which was 1280 × 960 with 140 depth steps, on a machine equipped with an Intel i7-3770 CPU and 16GB RAM with CPU parallelization. The computation times for estimating the depth map from six refractive inputs was about 77 s for the first stage of refractive stereo and about 33 s for the second-half stage of stereo fusion. The total computation time on runtime is about 110 s We precomputed the refracted essential points per pixel in the image plane beforehand for computational efficiency.

5.2. Evaluation of refractive calibration

Our refractive calibration method makes our system more efficient than our previous system [12], by enabling us to utilize any angle of the medium from a smaller number of measurements in calibration (see Section 3.2.2). For validation of our refractive calibration method, we compare the measured 36 essential points and the reconstructed essential points using our calibration method. We first evaluate the effects of the cardinality of sampled angles $|\Phi|$. The reconstruction error is defined as the arithmetic mean of L2 norms of the differences between the measured normals **n** and

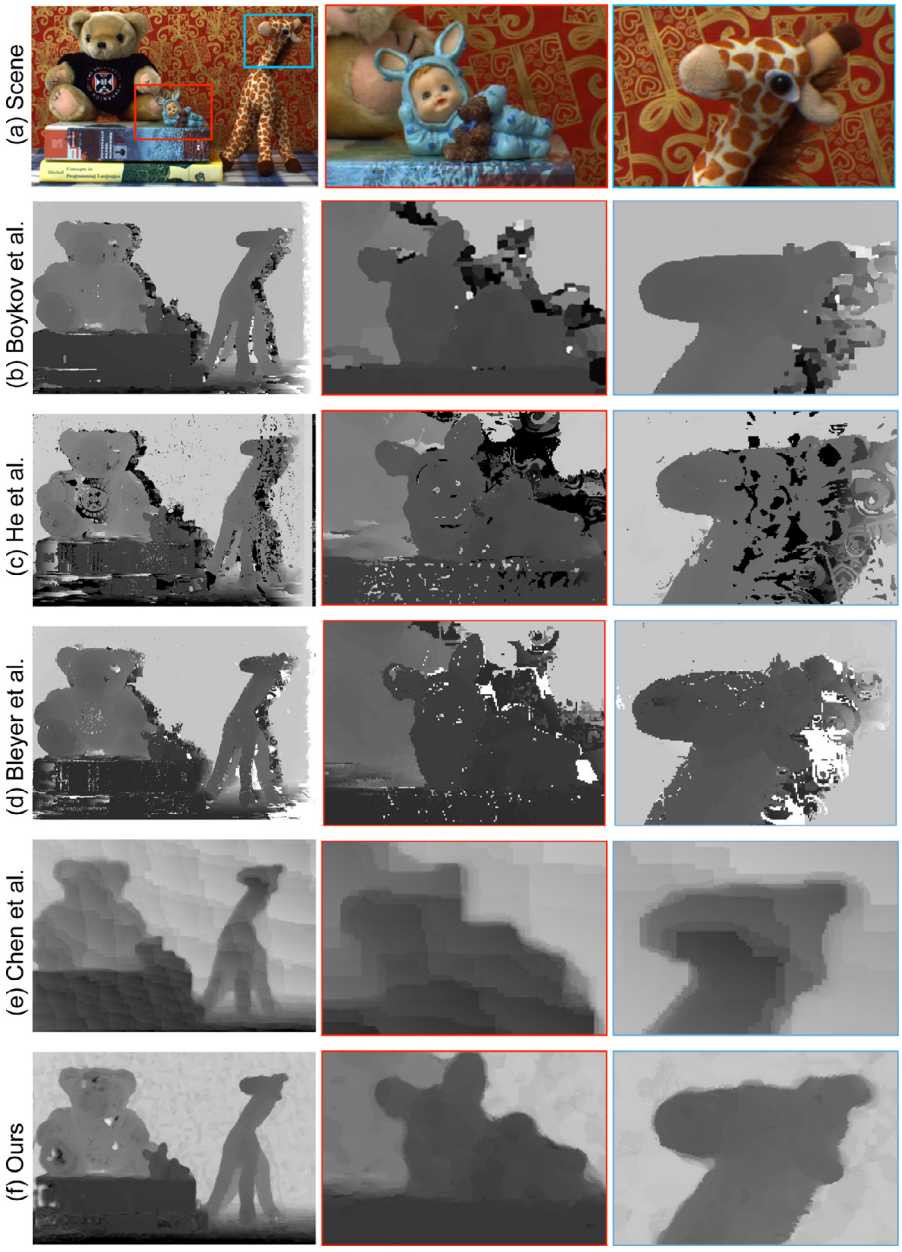

Fig. 15. Depth maps of a scene (a) are computed by five different methods. (b) and (c) show depth maps produced by global [38] and local binocular stereo [32] methods. (d) shows the depth maps obtained by a patchmatch-based binocular stereo method [39]. (e) presents depth maps produced by a refractive stereo method [10]. Our method (f) estimates depth accurately without suffering from severe artifacts.

the reconstructed normals $\hat{\mathbf{n}}$, obtained by Eqs. (10) and (12), respectively.

Fig. 12 (a) presents the measured 36 essential points (marked as circles), along with the reconstructed essential points (solid line), with nine sampled angles ($|\Phi| = 9$). Calibration error decreases rapidly up to nine samples, as shown in Fig. 12(b). We therefore chose nine angles for our calibration. We estimate two depth maps (see Fig. 12(c) and (d)): one from 36 measured essential points, and the other from 36 reconstructed points, with calibration of nine sampled angles.

5.3. Quantitative evaluation

The first row in Fig. 11 compares three different depth maps obtained by binocular only stereo (a), refractive only stereo (b) and our proposed stereo fusion method (c). Although the depth estimation of binocular only stereo (a) appears sound, (a) suffers from typical false matching artifacts around the edges of the front object due to occlusion. Refractive only stereo (b), obtained from the intermediate stage of our fusion method, presents depth without artifacts, but the depth resolution is significantly discretized and coarse. Our stereo fusion (c) overcomes the disadvantages of the homogeneous stereo methods. It estimates depth as well as binocular stereo without severe artifacts.

We quantitatively evaluated the accuracy of our stereo fusion method in comparison with the other methods in Fig. 11(d). We measured three points in the scene using a laser distance meter (Bosch GLM 80) and compared the measurements by the three methods. The accuracy of our method is as high as that of the binocular only method (averaged distance error: $\sim$ 2 mm), while it is superior to that of the refractive only method (aver. error: $\sim$ 6 mm).

5.4. Qualitative evaluation

The first rows (a) in Figs. 13, 14 and 15 present input images. The second rows (b) in these figures are results of the graphcut-based method [38]. The third rows (c) are results of a local binocular stereo method [32]. The fourth rows present results of a patchmatch-based stereo method [39]. Note that we utilize left and right images captured without any transparent medium as input for the compared binocular stereo methods [32,38,39]. The fifth rows (e) show results of a refractive stereo method [10]. The last rows (f) present results of our stereo fusion method.

We compared our proposed method with a renowned graphcut-based algorithm [38] with an image of the same resolution. Global stereo methods in general allow for an accurate depth map, while requiring high computational cost. It is not surprising that this global method was about eight times slower than our method, although it produces an elaborate depth map.

We also compared our method with two local binocular methods [32,39], which compute matching cost as the norm of the intensity difference. In binocular methods [32,39], the range of depth candidates is the same globally for every pixel. He et al. [32] produce depth maps with some notable artifacts, and it took about 212 s to compute, which is two times slower than our method. The patchmatch-based stereo method [39] presents depth accuracy similar to that of the graphcut-based algorithm [38]. It took about 720 s, which is slightly faster than the graphcut-based method [38]. Thanks to the reduced range in searching matching cost, our stereo fusion method outperforms other two local stereo methods in terms of computational time, without sacrificing depth accuracy.

A refractive method using SIFT flow [10] was also compared to ours. Six refractive images were employed for both methods. While the refractive method suffers from wavy artifacts caused by SIFT flow and its depth resolution is very coarse, typical of refractive stereo, our method estimates depth accurately with fewer spatial artifacts in all test scenes.

6. Future work

Our hardware design requires at least one rotation of the medium to obtain a depth map using more than two refracted images. The transparent medium was manually rotated in our experiments. It restricts the applications of our system to static scenes. Making the medium smaller and motorizing the rotation unit to apply our system to dynamic scenes remains to be explored in our future work.

Our pipeline currently consists of two stages: refractive depth estimation and stereo fusion. As our stereo fusion follows a coarse-to-fine approach, errors on the refractive depth map could be transferred to the final depth estimates. In our future work, we would like to resolve this problem by accounting for depth estimation and stereo fusion as a unified optimization problem to obtain a high-fidelity depth map.

Since optical refraction is related with spectral dispersion, we would like to apply our stereo fusion paradigm to hyperspectral imaging, exploiting refraction effects on spectral dispersion. We anticipate that the combination of hyperspectral imaging and refractive stereo imaging can broaden various fields of hyperspectral 3D imaging applications [40–43].

7. Conclusions

We proposed a novel optical design combining binocular and refractive stereo and introduced a stereo-fusion workflow. Our stereo fusion system is capable of estimating depth information with a high depth resolution and fewer artifacts at a speed that is competitive with other local and global binocular methods. We validated that our proposed method combines the advantages of both traditional binocular and refractive stereo. Also, our refractive calibration method makes our system more efficient than the previous method [12] by reducing the calibration cost of refractive stereo. Our quantitative and qualitative evaluation demonstrates that our fusion method outperforms the traditional homogeneous methods in terms of artifacts and depth resolution. In addition to these advantages, our stereo fusion can be easily integrated into any existing binocular stereo systems by simply introducing a transparent medium in front of a camera, allowing for a significant improvement in a depth map with fewer artifacts.

Acknowledgments

Min H. Kim, the corresponding author, gratefully acknowledges Korea NRF grants (2013R1A1A1010165 and 2013M3A6A6073718) and additional support by an ICT R&D program of MSIP/IITP (10041313).

References

[1] D. Scharstein, R. Szeliski, A taxonomy and evaluation of dense two-frame stereo correspondence algorithms, Int. J. Comput. Vis. 47 (1-3) (2002) 7–42.
[2] K. Kawashima, S. Kanai, H. Date, As-built modeling of piping system from terrestrial laser-scanned point clouds using normal-based region growing, J. Comput. Des. Eng. 1 (1) (2014) 13–26.
[3] A. Kadambi, R. Whyte, A. Bhandari, L.V. Streeter, C. Barsi, A.A. Dorrington, R. Raskar, Coded time of flight cameras: sparse deconvolution to address multipath interference and recover time profiles, ACM Trans. Graph. 32 (6) (2013) 167.
[4] A. Levin, R. Fergus, F. Durand, W.T. Freeman, Image and depth from a conventional camera with a coded aperture, ACM Trans. Graph. 26 (3) (2007) 70:1–9.
[5] C. Rhemann, A. Hosni, M. Bleyer, C. Rother, M. Gelautz, Fast cost-volume filtering for visual correspondence and beyond, in: Proceedings of the Computer Vision and Pattern Recognition (CVPR), IEEE, 2011, pp. 3017–3024.
[6] M. Okutomi, T. Kanade, A multiple-baseline stereo, IEEE Trans. Pattern Anal. Mach. Intell. 15 (4) (1993) 353–363.
[7] F. Zilly, C. Riechert, M. Müller, P. Eisert, T. Sikora, P. Kauff, Real-time generation of multi-view video plus depth content using mixed narrow and wide baseline, J. Vis. Commun. Image Represent. 25 (4) (2013) 632–648.
[8] C. Gao, N. Ahuja, Single camera stereo using planar parallel plate, in: Proceedings of the International Conference on Pattern Recognition (ICPR), 4, 2004, pp. 108–111.
[9] C. Gao, N. Ahuja, A refractive camera for acquiring stereo and super-resolution images, in: Proceedings of the Computer Vision and Pattern Recognition (CVPR), 2006, pp. 2316–2323.
[10] Z. Chen, K.-Y.K. Wong, Y. Matsushita, X. Zhu, Depth from refraction using a transparent medium with unknown pose and refractive index, Int. J. Comput. Vis. 102 (1-3) (2013) 3–17.
[11] Y. Nakabo, T. Mukai, Y. Hattori, Y. Takeuchi, N. Ohnishi, Variable baseline stereo tracking vision system using high-speed linear slider, in: Proceedings of the International Conference on Robotics and Automation (ICRA), 2005, pp. 1567–1572.
[12] S.-H. Baek, M.H. Kim, Stereo fusion using a refractive medium on a binocular base, in: Proceedings of the Asian Conference on Computer Vision (ACCV 2014), in: Vol. 9004 of Lecture Notes in Computer Science (LNCS), Springer, Singapore, Singapore, 2015, pp. 503–518.
[13] Y. Furukawa, J. Ponce, Accurate, dense, and robust multiview stereopsis, IEEE Trans. Pattern Anal. Mach. Intell. 32 (8) (2010) 1362–1376.
[14] D. Gallup, J.-M. Frahm, P. Mordohai, M. Pollefeys, Variable baseline/resolution stereo, in: Proceedings of the Computer Vision and Pattern Recognition (CVPR), 2008, pp. 1–8.
[15] S.M. Seitz, B. Curless, J. Diebel, D. Scharstein, R. Szeliski, A comparison and evaluation of multi-view stereo reconstruction algorithms, in: Proceedings of the Computer Vision and Pattern Recognition (CVPR), 2006, pp. 519–528.
[16] E. Hecht, Optics, Addison-Wesley, Reading, Mass, 1987.
[17] Y. Nishimoto, Y. Shirai, A feature-based stereo model using small disparities, in: Proceedings of the Computer Vision and Pattern Recognition (CVPR), 1987, pp. 192–196.
[18] D. Lee, I. Kweon, A novel stereo camera system by a biprism, IEEE Trans. Robot. Autom. 16 (5) (2000) 528–541.
[19] M. Shimizu, M. Okutomi, Reflection stereo-novel monocular stereo using a transparent plate, in: Proceedings of the Canadian Conference Computer and Robot Vision (CRV), IEEE, 2006.14–14
[20] M. Shimizu, M. Okutomi, Monocular range estimation through a double-sided half-mirror plate, in: Proceedings of the Canadian Conference Computer and Robot Vision (CRV), IEEE, 2007, pp. 347–354.

[21] Z. Chen, K. Wong, Y. Matsushita, X. Zhu, M. Liu, Self-calibrating depth from refraction, in: Proceedings of the International Conference on Computer Vision (ICCV), 2011, pp. 635–642.
[22] D.G. Lowe, Distinctive image features from scale-invariant keypoints, Int. J. Comput. Vis. 60 (2) (2004) 91–110.
[23] C. Liu, J. Yuen, A. Torralba, Sift flow: dense correspondence across scenes and its applications, IEEE Trans. Pattern Anal. Mach. Intell. 33 (5) (2011) 978–994.
[24] Z. Zhang, A flexible new technique for camera calibration, IEEE Trans. Pattern Anal. Mach. Intell. 22 (11) (2000) 1330–1334.
[25] S.J. Gortler, Foundations of 3D Computer Graphics, MIT Press, London, 2012.
[26] R.A. Waltz, J.L. Morales, J. Nocedal, D. Orban, An interior algorithm for nonlinear optimization that combines line search and trust region steps, Math. Program. 107 (3) (2006) 391–408.
[27] M.H. Kim, J. Kautz, Characterization for high dynamic range imaging, Comput. Graph. Forum (Proc. EUROGRAPHICS 2008) 27 (2) (2008) 691–697.
[28] R.T. Collins, A space-sweep approach to true multi-image matching, in: Proceedings of the IEEE Computer Society Conference on Computer Vision and Pattern Recognition, 1996. CVPR'96, IEEE, 1996, pp. 358–363.
[29] C. Kim, H. Zimmer, Y. Pritch, A. Sorkine-Hornung, M. Gross, Scene reconstruction from high spatio-angular resolution light fields, ACM Trans. Graph. 32 (4) (2013) 73:1–12.
[30] R.O. Duda, P.E. Hart, Pattern Classification and Scene Analysis, Wiley, 1973.
[31] D. Comaniciu, P. Meer, Mean shift: a robust approach toward feature space analysis, IEEE Trans. Pattern Anal. Mach. Intell. 24 (5) (2002) 603–619.
[32] K. He, J. Sun, X. Tang, Guided image filtering, in: Proceedings of the European Conference on Computer Vision (ECCV), Springer, 2010, pp. 1–14.
[33] S. Mattoccia, S. Giardino, A. Gambini, Accurate and efficient cost aggregation strategy for stereo correspondence based on approximated joint bilateral filtering, in: Proceedings of the Asian Conference on Computer Vision (ACCV), Springer, 2010, pp. 371–380.
[34] K.-J. Yoon, I.S. Kweon, Adaptive support-weight approach for correspondence search, IEEE Trans. Pattern Anal. Mach. Intell. 28 (4) (2006) 650–656.
[35] Z. Ma, K. He, Y. Wei, J. Sun, E. Wu, Constant time weighted median filtering for stereo matching and beyond, in: Proceedings of the International Conference on Computer Vision (ICCV), 2013, pp. 1–8.
[36] S.T. Barnard, Stochastic stereo matching over scale, Int. J. Comput. Vis. 3 (1) (1989) 17–32.
[37] J.-S. Chen, G. Medioni, Parallel multiscale stereo matching using adaptive smoothing, in: Proceedings of the European Conference on Computer Vision (ECCV), 1990, pp. 99–103.
[38] Y. Boykov, O. Veksler, R. Zabih, Fast approximate energy minimization via graph cuts, IEEE Trans. Pattern Anal. Mach. Intell. 23 (11) (2001) 1222–1239.
[39] M. Bleyer, C. Rhemann, C. Rother, Patchmatch stereo-stereo matching with slanted support windows., in: BMVC, 11, 2011, pp. 1–11.
[40] G. Nam, M.H. Kim, Multispectral photometric stereo for acquiring high-fidelity surface normals, IEEE Comput. Graph. Appl. 34 (6) (2014) 57–68.
[41] H. Lee, M.H. Kim, Building a two-way hyperspectral imaging system with liquid crystal tunable filters, in: Proceedings of the International Conference on Image and Signal Processing (ICISP) 2014, Lecture Notes in Computer Science, 8509, Springer, Normandy, France, 2014, pp. 26–34.
[42] M.H. Kim, T.A. Harvey, D.S. Kittle, H. Rushmeier, J. Dorsey, R.O. Prum, D.J. Brady, 3D imaging spectroscopy for measuring hyperspectral patterns on solid objects, ACM Trans. Graph. (Proc. SIGGRAPH 2014) 31 (4) (2012) 38:1–11.
[43] M.H. Kim, H. Rushmeier, J. ffrench, I. Passeri, D. Tidmarsh, Hyper3d: 3d graphics software for examining cultural artifacts, ACM J. Comput. Cult. Herit. 7 (3) (2014) 1:1–19.